OPTIMIZATION OF COOLING STRUCTURE AND ANALYSIS OF FLOW THERMAL PERFORMANCE FOR HIGH-SPEED PERMANENT MAGNET MOTOR IN HYDROGEN FUEL CELL AIR COMPRESSORS

Jinhui LIU[1], Longwei WANG[1], Haoqiang YANG[1], Xiaobo SUN[1], Minghui WANG[1*]

[*1]School of Electrical and Electronic Engineering, Harbin University of Science and Technology, Harbin 150080, China

[*] Corresponding author; E-mail: wmh_hrbust@163.com

In order to investigate the impact of the cooling system design on the thermal dissipation performance of a high-speed permanent magnet synchronous motor (HPMSM), a 10-kW HPMSM for a hydrogen fuel cell compressor is taken as the research object. Drawing upon fluid mechanics and fluid-structure interaction (FSI) heat transfer theory, multiple cooling water circuit configurations are designed, and their flow velocity, pressure, and temperature rise characteristics are compared to initially identifying the more superior structure. In this paper, the influence of the number of water channels and the cooling medium flow velocity on the fluid and temperature field are studied, revealing the cooling medium's rheological behavior and temperature rise distribution under optimal conditions. Through simulation result comparisons and experimental verification, an optimal cooling structure is proposed to effectively optimize the temperature distribution and enhance cooling performance. This study offers theoretical support and engineering reference for cooling system design of HPMSMs in hydrogen fuel cell air compressors.

1. Introduction

In the context of global energy shortages and climate warming, hydrogen fuel cells have gained significant market favor due to their high efficiency, pollution-free and rapid fuel replenishment capabilities, with the growing demands [1]. High-speed permanent magnet synchronous motors (HPMSMs), characterized by high power density, high power factor, and compact structure, are widely used in hydrogen fuel cell air compressors [2-3]. As the important power component, the speed, power, efficiency and weight are notable at present. Consequently, the heat dissipation conditions [4] during operation have become more demanding, often leading to elevated temperatures and demagnetization of permanent magnets [5]. This not only decreases efficiency but also shortens curtails the lifespan. Therefore, the rational design of the motor cooling system is of utmost importance.

Many scholars at home and abroad have conducted research on the temperature rise of large motors [6-9]. The temperature rise of permanent magnet synchronous motors (PMSMs) is primarily investigated using methods such as the finite element method (FEM) [10], lumped parameter thermal network method [11], finite difference method [12] and analytical method [13]. For instance, a three-dimensional fluid-solid coupling heat transfer model for a compressor was established by [14], where the flow law of the cooling medium and the temperature distribution of armature windings under different inlet wind speeds were analyzed. In [15], an electromagnetic thermal coupling method for water-cooled permanent magnet motor was presented, which accounts for assembly gap in thermal analysis and improved the calculation accuracy of motor losses and temperature rise. In [16], the modeling and separation methods of losses in each component of high-speed motor have been analyzed.

To ensure reliable motor operation, designing a reasonable cooling structure grounded in precise temperature distribution calculations is essential. Common motor cooling methods include air cooling [17], oil cooling [18] and water cooling [19]. For new energy-driven motors, water cooling offers advantages over air cooling, such as higher heat dissipation density, low noise and independent cooling system, making it widely adopted [20]. Although placing water channels close to the winding aids cooling, this can increase losses. Thus, water channels are typically integrated into the housing [21]. [22] designed various water channel cooling structures and analyzed their temperature field via magneto-thermal coupling, demonstrating that water-cooling systems effectively reduced the winding temperature. [23-24] indicate that the heat dissipation performance of water channels depends on the convective heat transfer coefficient and convective area, and deduced the influence of cooling medium flow velocity and pipe dimensions on the convective heat transfer coefficient of spiral water channels. Reference [25] investigates the cooling efficiency of different nanofluids as water channel cooling media based on heat transfer theory and numerical simulation. The results demonstrated that nanofluids can significantly reduce the temperature rise of various motor components. In [26], an innovative cooling solution combining air cooling with an integrated water-cooling system is applied to air-cooled IM motors. By constructing a thermal simulation model and conducting numerical analysis, the cooling performance of the motor is effectively enhanced. Additionally, corresponding pump power requirements are calculated for different water flow conditions within the cooling system.

This paper investigates a 10kW high-speed permanent magnet synchronous motor for automotive applications. Three distinct cooling structures were designed, and the fluid flow fields, pressure fields, and temperature fields were compared to select the optimal cooling structure for the prototype. Subsequently, analytical and CFD methods were employed to reveal the influence mechanisms of water channel quantity and coolant velocity on convective heat transfer coefficient, convective heat exchange area, channel pressure drop, and motor temperature rise. Based on these findings, an optimal cooling structure scheme is proposed to achieve the design goal of low temperature rise. Finally, motor temperature rise experiments validate the rationality of the cooling structure design and the accuracy of the temperature rise simulation analysis method.

2. Proto parameterization and solution modeling

2.1. Basic motor parameters

In this study, a 10-kW-high-speed permanent magnet synchronous motor for air compressor for hydrogen fuel cell is studied as an example, and the basic parameters of the motor are shown in Table 1. The cooling structure design and optimization flow chart of this paper is shown in Fig. 1

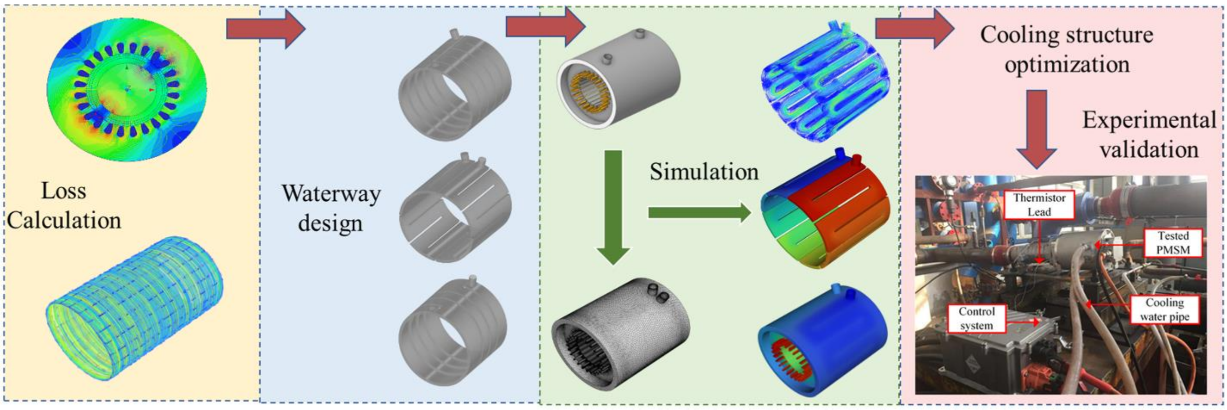

Figure 1. Flow chart for cooling structure design and optimization

Table 1. The basic parameters of the proto

Parameters	Value
Rated power (Kw)	10
Rated RPM (r/min)	15000
Rated voltage (V)	380
Number of stator slots	24
Number of poles	2
Outer diameter of stator (mm)	135
Stator inner diameter (mm)	68

In this study, the electromagnetic loss of the motor is simulated based on the finite element method, and the results of the finite element analysis are shown in Table 2.

Table 2. Losses in each part of the motor

Loss of components (W)	Copper loss	Stator core loss	Eddy current loss	Wind friction loss
Value	141.5	156.8	17	11.2

2.2. Cooling waterway design

Typically, cooling waterway structure can be categorized into two primary types: axial cooling water channels and circumferential cooling water channels. For the circumferential spiral waterway, the cooling medium enters the motor from the inlet and flows spirally along the circumferential direction before being discharged from the outlet. The axial foldback waterway features inlets and outlets positioned on the same horizontal plane, with the cooling medium flowing axially in a folded path toward the outlet. In the circumferential foldback water channel, the inlet and outlet are located at the top and bottom on the same side of the motor, and the cooling medium flows reciprocally in the circumferential direction for discharge. The configurations of the three water channels structures are illustrated in Fig. 2.

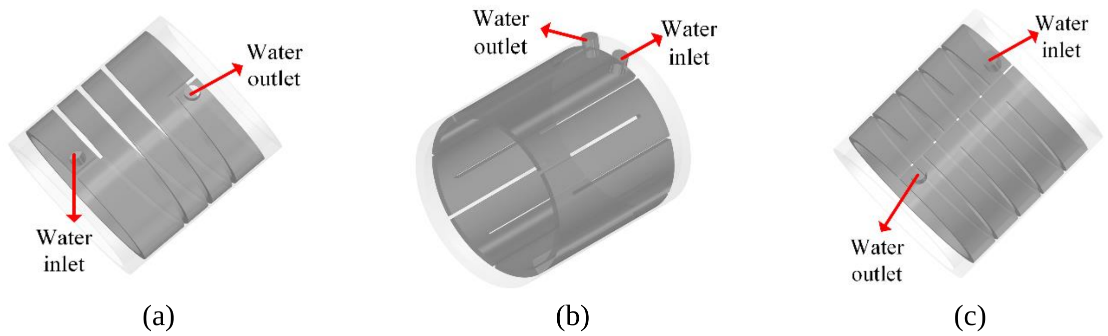

Figure 2. (a) circumferential spiral; (b) axial foldback; (c) circumferential foldback

During the water channel design process, it is crucial to ensure that parameters such as hydraulic diameter, waterway height, and internal surface area are fundamentally consistent across the three waterway structures. This makes it easier for us to study the cooling performance of different waterway structures more accurately. The designed cooling water channels parameters are tabulated in Table 3.

Table 3. Cooling waterway parameters

Waterway parameters	Circumferential spiral	Axial foldback	circumferential foldback
internal surface area （mm^2）	136544	136039	136501
Number of waterways	5	16	5
Inlet and outlet diameter (mm)	14	14	14
Waterway height (mm)	6	6	6
Waterway spacing (mm)	3	3	3
Waterway axial length (mm)	135	135	135

2.3. Motor Simulation Modeling and Boundary Condition Setting

Considering the minimal loss generated by the rotor and permanent magnet during the operation of the permanent magnet synchronous motor, the simulation model of the motor is simplified and designed under the premise of ensuring the calculation accuracy. The simplified three-dimensional solution model of the motor is depicted in Fig. 3 (a).

To enhance the resolution accuracy of the boundary layer, the fluid domain employs a three-dimensional expanded-layer boundary grid. The primary grid cell size is set to 2 mm, with the boundary layer configured as 3 layers and a growth rate of 1.2, as illustrated in Fig. 3 (b).

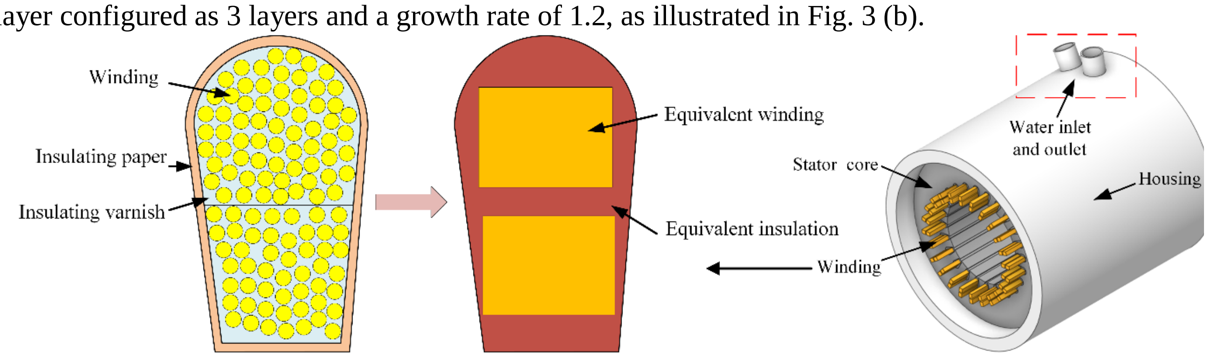

(a)

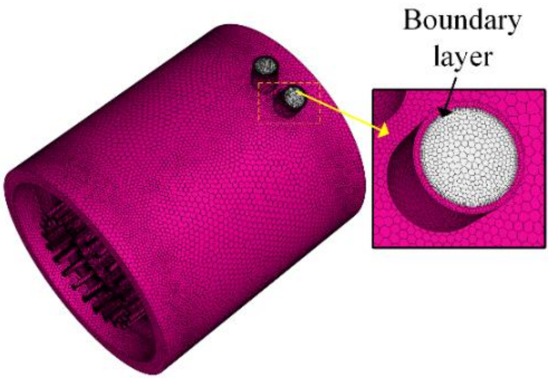

(b)

Figure 3. (a)Motor 3D solution model; (b) Mesh profiling

To streamline the fluid-structure interaction computational process, the following assumptions are incorporated into the solution model:

• Introduction of an equivalent conductor replacing the copper wires of the winding and an equivalent insulation layer for all insulating materials in the slot;

• The fluid flow state in the cooling water channels is assumed to be unaffected by buoyancy and gravity;

• To facilitate simulation and analysis, the heat source are applied exclusively to the inner surface of the casing and the winding.

Since the fluid flow in this study is turbulent, the RNG k-e turbulence model is selected for calculations. Before computation, accurate boundary conditions must be set for the motor model:

• Input the density, viscosity, variable thermal conductivity, and thermal conductivity of the cooling medium;

• A uniform flow velocity of 0.1 m/s is specified at the inlet of all three water channels;

• The inlet and outlet temperatures of the water channels are set to 30°C;

• The outlet is defined as a pressure outlet with an initial pressure of 1 atmosphere;

• All solid surfaces in contact with the fluid are assigned no-slip boundary conditions.

3. Numerical solution calculations

3.1. Fluid field and temperature field analysis under three cooling structure schemes

Fig. 4 illustrates flow velocity distribution in different water channels. Fig. 4(a) shows a circumferential spiral water channel with high flow velocity at the inlet and outlet, with uniform flow velocity in the middle water channel, reaching a maximum of 0.18 m/s; Fig. 4(b) shows the axial foldback water channel, where the fluid undergoes multiple turns, generating obvious turbulence and non-uniform flow velocity distribution. The maximum velocity of 0.27 m/s is concentrated in the inner corners; Fig. 4(c) depicts a circumferential water channel, featuring high flow velocity at the lateral side of the water channel and regular distribution overall, with a maximum velocity of 0.28 m/s. Comparison reveals that the circumferential spiral water channel enables uniform heat dissipation, its flow velocity remains relatively low. In contrast, the axial foldback and circumferential foldback water channels achieve higher flow velocities due to the multiple turns, but the flow velocity decreases dramatically outside of the water channel corners, potentially causing heat dissipation inefficiencies in certain areas.

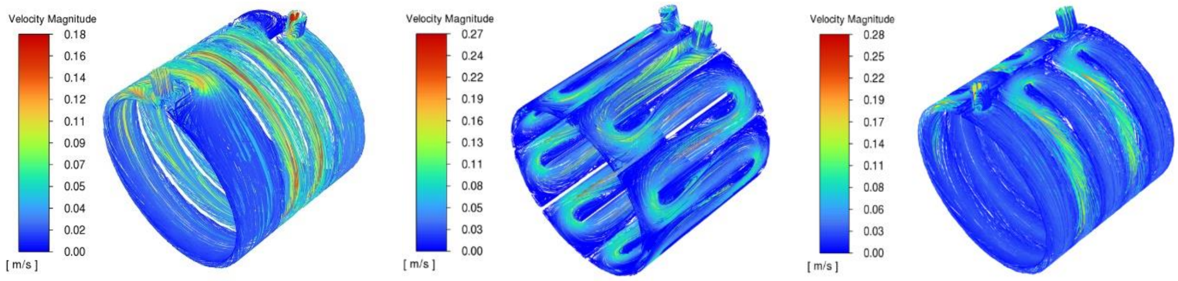

(a) circumferential spiral (b) axial foldback (c) circumferential foldback

Figure 4. Flow velocity distribution in different water channels

Fig. 5 illustrates the pressure distribution in different water channels. As shown in Fig. 5(a), the circumferential spiral water channel exhibits higher pressure in the transition zone near the inlet, with pressure decreasing sequentially along the channel, resulting in a maximum pressure difference of 178.3 Pa; In Fig. 5(b), the circumferential foldback water channel demonstrates the highest pressure in the first two channel sections and at the inlet, with a maximum pressure difference of 548.6 Pa. Fig. 5(c) reveals that the axial foldback water channel has higher pressure in the inlet section and the first channel section, with a maximum pressure difference of 331.1 Pa. The pressure differences of the three structures are ranked in descending order as follows: circumferential spiral, circumferential foldback, and axial foldback.

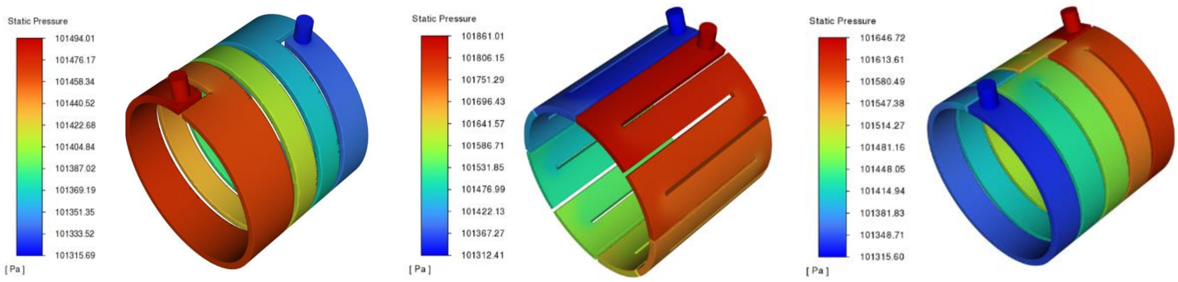

(a) circumferential spiral (b) axial foldback (c) circumferential foldback

Figure 5. Pressure distribution in different water channels

Fig. 6 illustrates the temperature distribution of the motor under different configurations of water channels. The situation with the circumferential spiral water channels exhibits a maximum temperature of 90.94°C; the situation with the axial foldback water channels reaches a maximum temperature of 87.84°C; and the situation with the circumferential foldback water channels records a maximum temperature of 90.7°C.

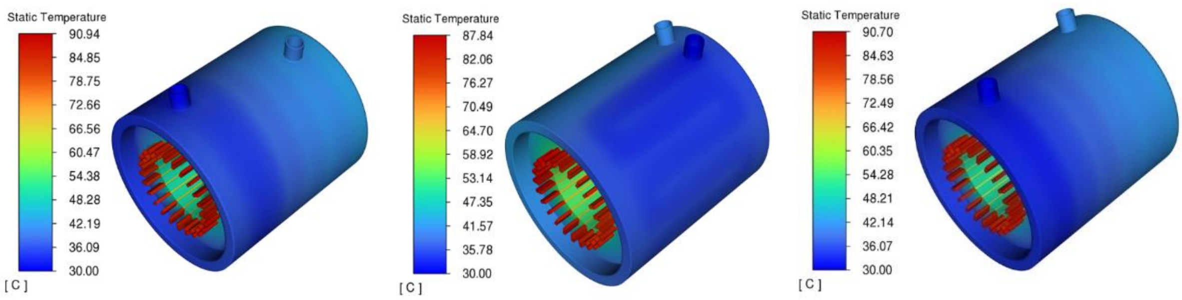

(a) circumferential spiral (b) axial foldback (c) circumferential foldback

Figure 6. Temperature cloud for the three water channel scenarios

Based on the simulation results above, the axial foldback channel design offers multiple advantages that optimize its heat dissipation performance: First, its turning channel structure disrupts the fluid boundary layer to generate turbulence, which achieving a maximum flow velocity of 0.27 m/s, significantly enhancing heat exchange rates; Second, although its inlet-outlet pressure difference exceeds other channel designs, the moderate pressure drop ensures sufficient cooling medium flow momentum, preventing insufficient velocity while keeping pump power requirements within engineering limits. Third, its inlet-outlet alignment on the same horizontal plane and axial distribution along the housing adapts to compact installation spaces, while adjustable channel spacing ensures optimal stator contact. Through comprehensive evaluation of thermal performance, system energy consumption, and structural compatibility, this study ultimately selected the axial return channel design to enhance cooling efficiency and ensure reliable motor operation.

4. Structural Optimization Study of Axial Foldback Waterways

4.1. Analytical calculation of the effect of the number of waterways on heat dissipation and flow resistance

The number of waterways affects the convective heat dissipation area immediately, and the relationship between the convective heat dissipation area of axial foldback waterways and the number of waterways is:

$$A_\alpha = \left[\frac{\pi D l}{n} - h_w l + 2hl \right] \cdot n \tag{1}$$

where n is the number of water channels, A_α is the waterway heat exchange area, D is the average diameter of the water channel, h_w is the width of the interval between adjacent water channels, l is the length of a single linear water channel, and h is the height of the water channel.

The relationship between the waterway convection heat transfer coefficient and n is:

$$\begin{cases} Re_f = \dfrac{v_l d_e}{v_f} \\ \eta = \dfrac{Nu_f \lambda_f}{d_e} \end{cases} \tag{2}$$

where Re_f is the Reynolds number of the fluid, η is the convective heat transfer coefficient, v_l is the flow velocity, v_f is the kinematic viscosity of the fluid, d_e is the hydraulic diameter, Nu_f is the Nusselt number of the fluid, and λ_f is the thermal conductivity of the fluid.

$$\begin{cases} Nu_f = 7.49 - 17.02 \cdot \dfrac{h}{w} + 22.43 \cdot \left(\dfrac{h}{w}\right)^2 - 9.94 \cdot \left(\dfrac{h}{w}\right)^3 + \dfrac{0.064 \cdot \left(\dfrac{d_e}{L}\right) \cdot Re_f \cdot Pr_f}{1 + 0.04 \cdot \left(Re \cdot Pr_f \cdot \dfrac{d_e}{L}\right)^{2/3}} & Re_f \le 2320 \\ Nu_f = 0.012 (Re_f^{0.87} - 280) Pr_f^{0.4} \cdot \left[1 + \left(\dfrac{d_e}{L}\right)^{\frac{2}{3}}\right] \left(\dfrac{Pr_f}{Pr_w}\right)^{0.11} & Re_f > 2320 \end{cases} \tag{3}$$

where w is the width of the channel, L is the length of the channel, and Pr_w is the Prandtl number of the fluid.

The total pressure drop of a fluid flowing through an axial foldback waterway is:

$$\Delta P = \Delta P_h + \Delta P_j \tag{4}$$

$$\Delta P_h = \lambda \frac{L}{d_e} \frac{v^2}{2g} \tag{5}$$

$$\Delta P_j = \zeta \frac{v^2}{2g} \tag{6}$$

where ΔP is the total pressure drop, ΔP_h is the along-track pressure drop, ΔP_j is the local pressure drop, λ is the along-track friction coefficient, g is the gravitational acceleration, and ζ is the local pressure loss coefficient.

When the fluid passes through an L-shaped corner pipe, ζ is calculated by the following equation:

$$\zeta = \lambda \cdot \frac{L_{eq}}{d_e} \tag{7}$$

where L_{eq} is the equivalent length of the corner waterway.

Based on the above equations, Fig. 7(a) and 7(b) are derived. A_α and η exhibit a direct proportion relationship with n. Namely, as n increases, the cooling performance of the water channel improved. However, the channel pressure drop demonstrates a nonlinear growth trend with the increase of n, where the growth rate gradually accelerates, exhibiting distinct acceleration characteristics. As the pressure drop increases, the improvement in heat dissipation performance gradually diminishes. Since the pump power is proportional to the pressure drop in the water channels, excessive pressure drop leads to increased operational energy consumption of the cooling system, thereby reducing the cost-effectiveness of heat dissipation. Additionally, excessive pressure drop can create stagnant zones in dead corners of the cooling channels. Slow-moving coolant in these stagnant areas may form hot spots. Furthermore, prolonged operation of the cooling channels under excessive pressure drop accelerates pump wear, shortens the service life of the cooling channels, and ultimately compromises motor reliability. Therefore, a larger value of n does not inherently translate to superior performance. Consequently, the number of water channels selected in this study is constrained to be less than 30.

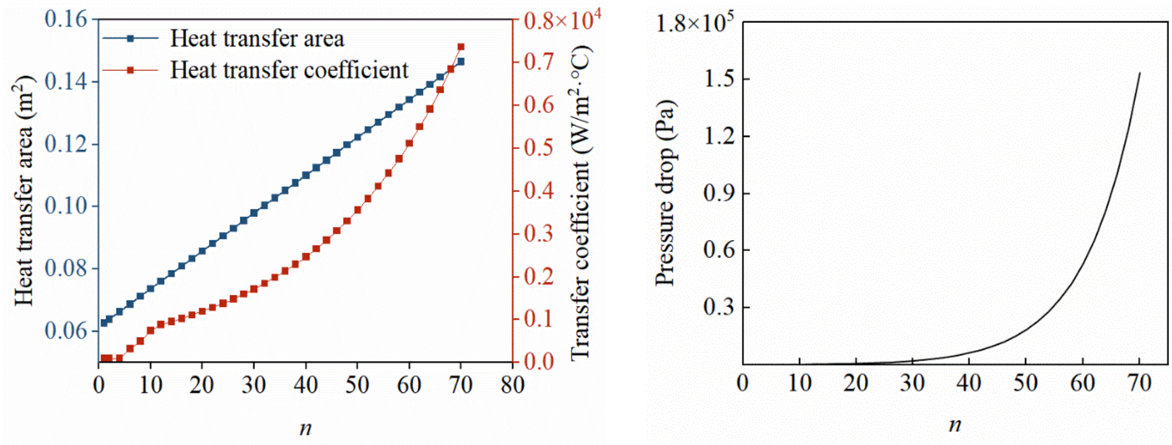

(a) (b)

Figure 7. (a) Variation of heat transfer area on the number of water channels; (b) Variation of heat transfer coefficient with the number of water channels

4.2. Simulation of motor fluid and temperature fields for different number of waterways

Following theoretical derivations and preliminary designs, axial folding water channels with n of 4, 8, 12, 20, 24 and 28 are selected for simulation calculation and analysis. During the simulations, all parameters are held constant except n, enabling the analysis of temperature, fluid flow, and pressure fields across varying n configurations to determine the optimal channel count.

Fig. 8 depicts the flow velocity distribution within the water-cooled motor under different n. For a fixed inlet velocity, increasing n leads to a proportional increase in the cooling medium's flow velocity within the channels. The maximum flow velocity in the axial foldback structure waterway increases from 0.22m/s at n=4 to 0.42m/s at n=28.

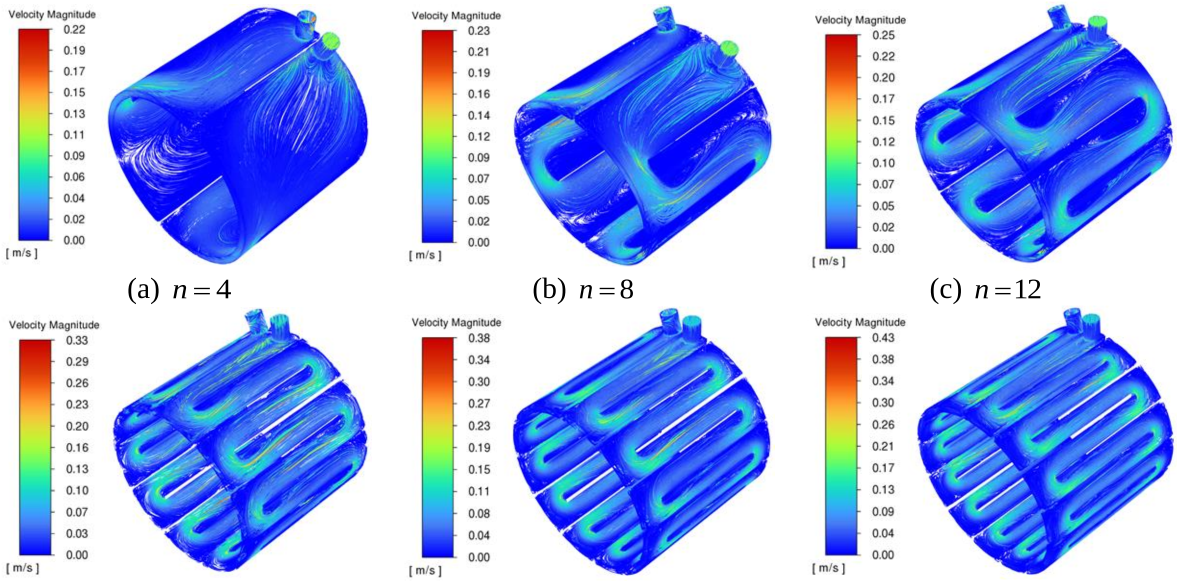

(a) $n=4$ (b) $n=8$ (c) $n=12$

(d) $n=20$ (e) $n=24$ (f) $n=28$

Figure 8. Distribution of flow velocities in sewers with different number of water channels

Fig. 9 presents the pressure field distribution of the motor with varying numbers of water channels. As the number of water channels increases, the drop of pressure across the axial foldback water channels gradually rises from 110.8 Pa at n=4 to 2149.18 Pa at n=28. The maximum pressure region is concentrated at the inlet, where the resistance to fluid flow increases sharply. Consequently, when determining the optimal number of water channels, the impact of pressure drop must be carefully considered to achieve better heat dissipation performance.

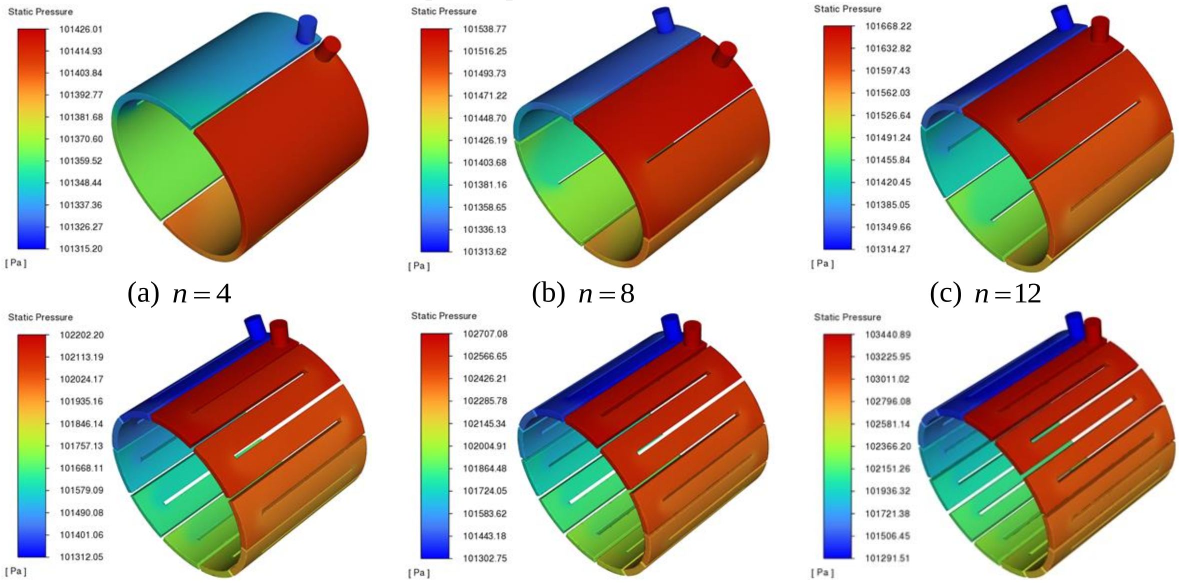

(a) $n=4$ (b) $n=8$ (c) $n=12$

(d) $n=20$ (e) $n=24$ (f) $n=28$

Figure 9. Pressure distribution of sewers with different numbers of water channels

Fig. 10 illustrates the temperature distribution of the water-cooled motor with axial foldback channel structure for varying number of channels. As depicted in Fig. 10, the maximum temperature decreases with an increase in the number of fluid-flows water channels. When the number of water channels increases from n=4 to n=20, the maximum temperature decreases by 4.68°C. Conversely, when the number of water channels increases from n=20 to n=28, the maximum temperature decreases by only 0.48°C. This phenomenon is attributed to the longer flow path of the cooling medium within the water channels, which causes the medium to absorb more heat and results in a rise in the temperature of the downstream cold medium, thereby reducing the overall heat dissipation efficiency of the cooling system.

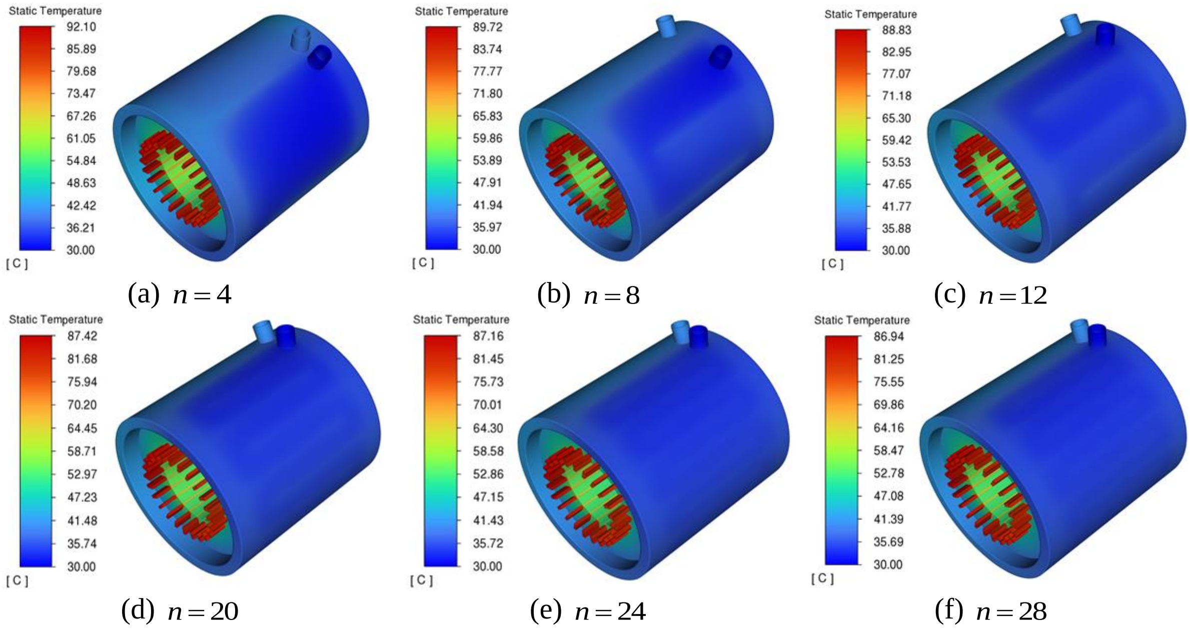

Figure 10. Temperature distribution of motors with different number of water channels

Fig. 11 depicts the internal temperature distribution of the motor for different water channels configurations, revealing that the cooling efficiency of the axial foldback water channels exhibits a tendency to decelerate with the increase in the number of water channels. This observation implies the existence of an optimal range for the number of water channels.

In summary, this study determines the number of axial foldback water channels to be 20, a configuration that not only ensures the heat dissipation performance of the water channels but also mitigates the risk of excessive pressure drop in the water channel system.

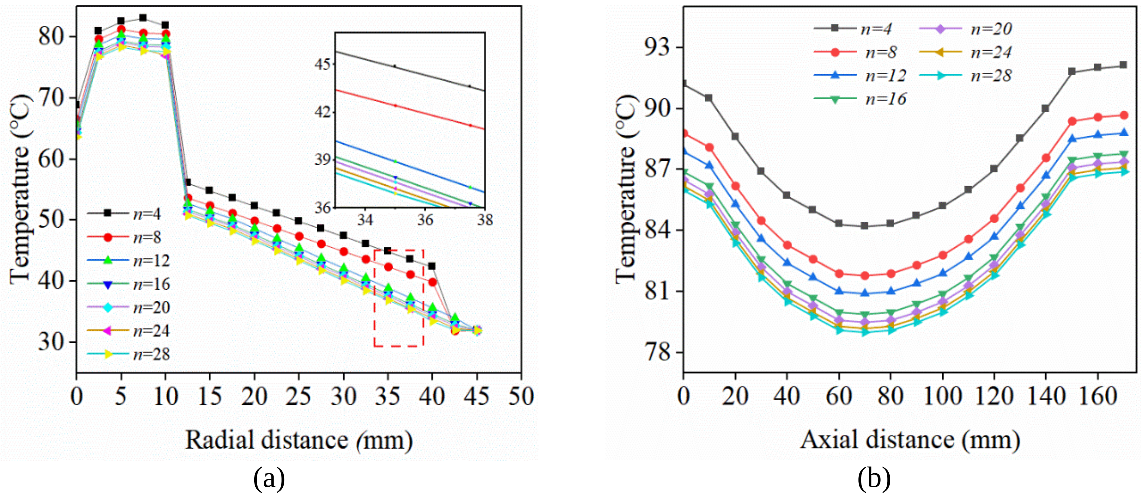

Figure 11. Motor temperature for different number of waterways (a) Motor radial cross-section temperature distribution; (b) Motor winding axial cross-section temperature distribution

4.3. Effect of cooling medium flow velocity on temperature and fluid fields

The flow state of the cooling medium is closely related to Re_f. When Re_f < 2000, the flow is laminar flow; when $2000 \le Re_f \le 4000$, it is transition flow; and when $Re_f > 4000$, it is turbulent flow.

According to the calculation of equation (2), the critical laminar flow velocity of the cooling medium is obtained as 0.19m / s, and the critical turbulent flow velocity is 0.39m / s. To determine the appropriate cooling medium flow velocity, multiple velocities are selected for simulation analysis of the temperature field and fluid field. The pressure drop variation curve of the water channel is shown on Fig. 12. The results indicate that when the flow velocity increases from 0.04 m/s to 0.19 m/s, the water channel drop of pressure increases by 2578.1 Pa; when the flow velocity further increases to 0.39 m/s, the drop of pressure moderately increases by 9210.5 Pa; when the flow velocity rises to 3.89 m/s, the drop of pressure sharply increases by 11692.2 Pa.

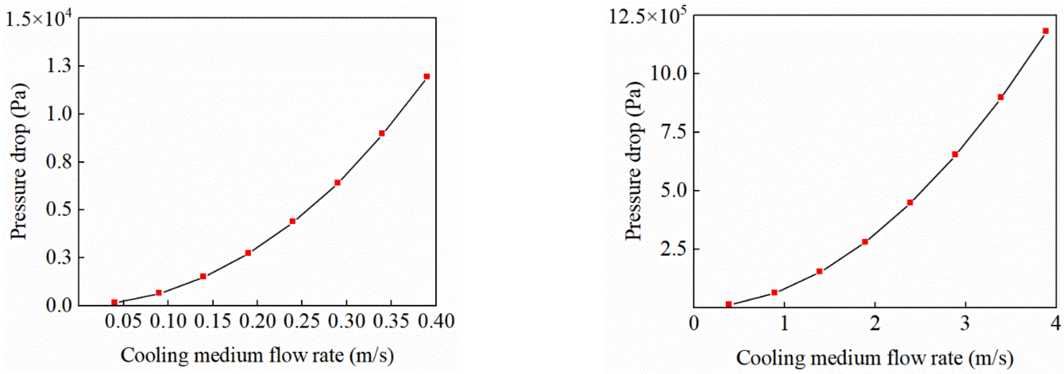

(a) (b)

Figure 12. (a) Changes in waterway pressure drop during laminar flow; (b) Changes in waterway pressure drop during turbulence

Figure 13 illustrates the influence of cooling medium flow velocity on the maximum temperature. The results reveal that as the flow velocity increases from 0.04 m/s to 0.19 m/s, the maximum temperature decreases by 19.9°C. When the flow velocity increases to 0.39 m/s, the temperature reduction amounts to 3.9°C. However, when the flow velocity reaches 3.89m/s, the temperature decreases by only is only 1.5°C, indicating that the heat dissipation capacity of the water channel has approached its limit, and further increase in flow velocity yield diminishing returns for heat dissipation enhancement. Consequently, this study designates 0.39 m/s as the optimal cooling flow velocity of axial folding water channel.

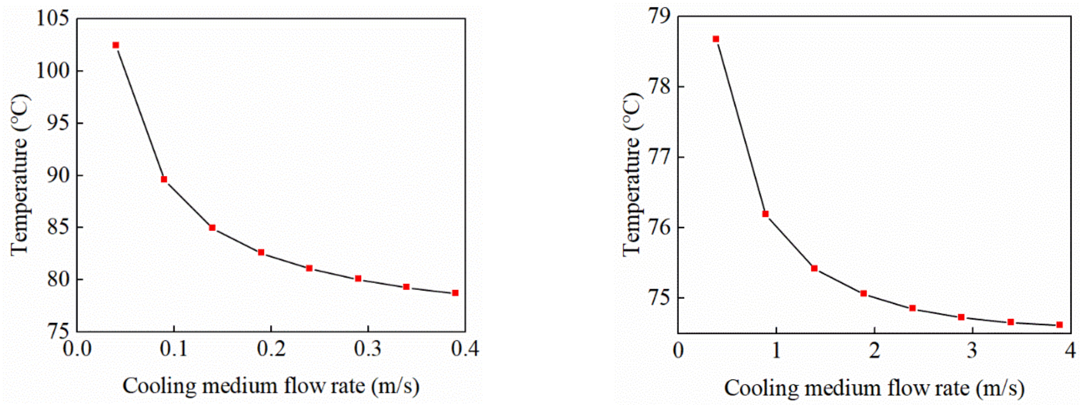

(a) (b)

Figure 13. (a) Maximum motor temperature during laminar flow; (b) Maximum motor temperature during turbulence

From the perspective of heat transfer and fluid mechanics coupling principles, there exists a positive correlation between cooling water channel pressure drop and heat dissipation performance. Therefore, compensating for pressure drop in cooling channels is essential when enhancing heat dissipation, particularly for axial foldback-type channels. This can be achieved through three approaches: First, optimize geometric parameters by incorporating reasonable radii at bends to reduce local vortex pressure drops, and control the length-to-diameter ratio of each channel segment to prevent excessive accumulation of ΔP_h. Second, match and adapt pumps whose output pressure offsets the total channel pressure drop while maintaining efficiency. Third, establish a coupled pressure drop-flow rate model to dynamically adjust pressure drop under fluctuating flow conditions, ensuring stable coolant velocity and ultimately achieving synergistic optimization of heat dissipation and pressure drop.

5. Experimental validation of the cooling scheme

Based on the above analysis, the optimal cooling system is adopted, and finite element simulation is performed on the motor investigated in this study. The simulation results of the temperature rising under the rated operating conditions are presented in Fig. 14. A notable radial temperature gradient is observed in the stator core: the yoke region exhibits lower temperatures, while the tooth region experiences higher temperature rise, with the maximum temperature reaching 43.9℃. Significant temperature disparity exists between the upper and lower windings, where windings adjacent to the tooth region show higher temperature rise, with the peak temperature reaching 71.9℃. The highest temperature of the sheath is located at its mid-section, reaching 56.5℃, and the temperatures of permanent magnets and sheath are essentially identical. Given that the maximum temperature of NdFeB permanent magnet is 180℃, which is much higher than the rated operating temperature. This indicates that the cooling system demonstrates excellent cooling performance and reliability.

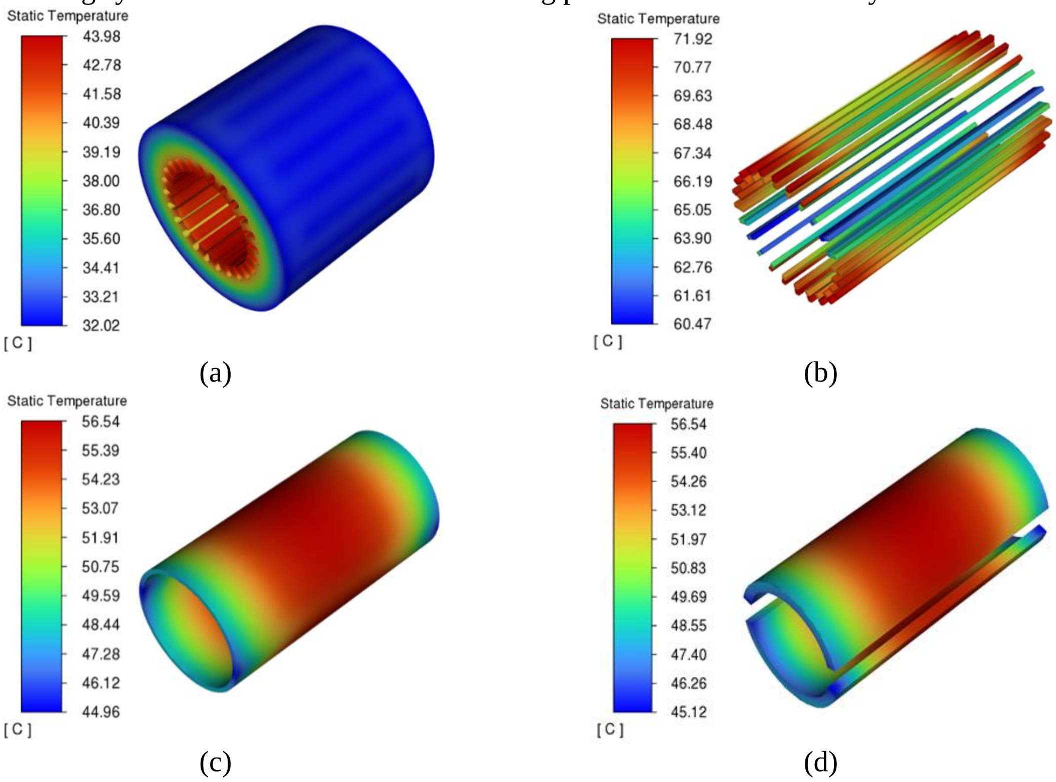

Figure 14. Motor temperature distribution (a) Stator core temperature. (b) Winding Temperature. (c) Sleeve temperature. (d) Permanent magnet temperature

5.1. Experimental verification

To validate the accuracy of the analysis method and the proposed cooling scheme, experiments of temperature rising are conducted on the proto platform. Fig. 15(a) illustrates the motor temperature rise experimental platform. The motor is tested under rated operating conditions at 15,000 r/min.

Stator winding temperatures are measured using the embedded thermocouple method, wherein thermocouple wires are embedded at the bottom of stator slots and at winding ends to obtain temperature rises at different winding locations. The temperature at this location represents the average temperature rise of the permanent magnet. Ambient temperature is measured using three thermometers uniformly distributed within a 1-meter radius around the motor. Their arithmetic mean serves as the ambient temperature for subsequent calculations of temperature rise at each location. Pressure sensors are installed at the inlet and outlet of the water channel to measure the pressure differential between the two points.

As depicted in Fig. 15(b), under the ambient temperature of 30 ℃, the temperature rise at the winding end was 40.6 ℃, compared with a simulation result of 41.9 ℃, yielding a 3.2% error. The experimental temperature rise at the bottom of the stator slot is 29.2 ℃, while the simulation result was 30.1 ℃, with an error of 3.1%. As shown in Fig. 15(c), the maximum temperature rise of the motor using circumferential spiral-type water channels was 43.9°C, with numerical simulation results at 45.7°C, representing an error of 4.1%. When using circumferential foldback -type water channels, the maximum temperature rise was 42.8°C, with numerical simulation results at 44.9°C, representing an error of 4.9%.These errors meet the engineering requirements, confirming the feasibility of the numerical simulation method and indirectly verifying the accuracy of the preceding analysis.

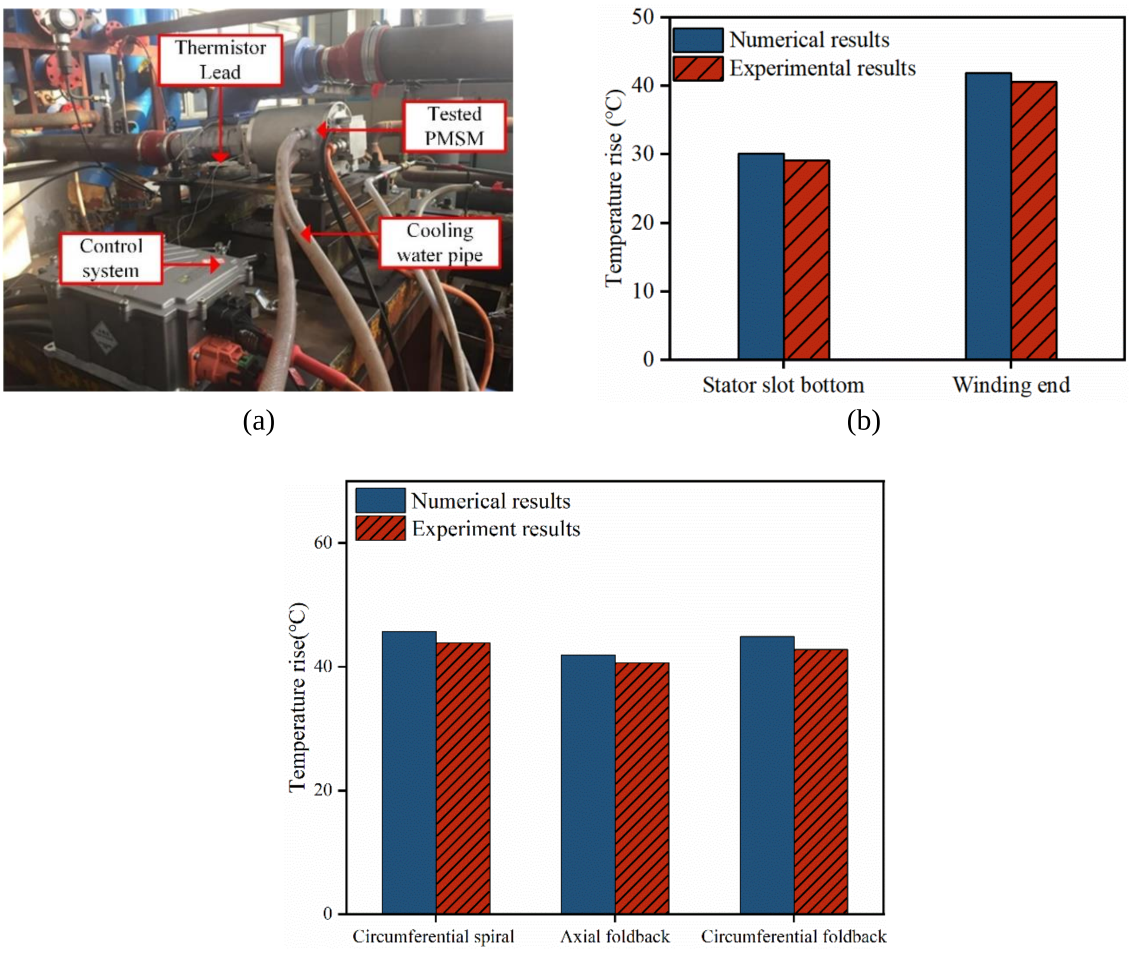

Figure 15. (a) Experimental platform; (b) Result validation;(c) Results from different channel experiments

6. Conclusion

In this study, a 10-kW permanent magnet synchronous motor for hydrogen fuel cell compressors is selected as the research object. Three cooling waterway structures are comparatively analyzed using computational fluid dynamics (CFD), and the axial folding waterway is identified as the optimal solution. Under identical operating conditions, the axial foldback-type channels exhibit a maximum temperature rise that is 5.1% lower than that of the circumferential spiral-type waterway and 4.7% lower than that of the circumferential foldback waterway. Meanwhile, an analytical model is established to characterize the quantitative relationships among the number of water channels, heat dissipation area, convective heat transfer coefficient, and pressure drop in the water channels. When the number of water channels increased from 12 to 20, the maximum temperature rise of the motor decreased by 8.3%. However, when the number of water channels further increased from 20 to 28, the maximum temperature rise decreased by only 1.9%, yet the pressure drop surged more than 24 times. This indicates that the cooling performance is optimal when the number of water channels is 20.

Additionally, the influence of cooling medium's flow regime on pressure drops and temperature rise is investigated. At the optimal flow velocity of 0.39 m/s, the motor's heat transfer efficiency drops to only 76.7% at 0.04 m/s. Moreover, around the turbulent critical velocity of 0.39 m/s, increasing the flow velocity from 0.38 m/s to 0.40 m/s results in a mere 1.1% improvement in heat transfer performance while significantly increasing resistance by 25.6%. It was discovered that when the cooling flow velocity approaches the turbulence critical zone, flow resistance can be controlled while maintaining good heat transfer performance, thereby achieving optimal cooling efficiency. Ultimately, the cooling medium flow velocity was determined to be 0.39 m/s. Temperature rise experiments conducted at this flow velocity showed good agreement between the temperature rise and thermal simulation results, thereby verifying the correctness of the simulation and theoretical analysis.

Future research will focus on deepening exploration of high-power-density water-cooled permanent magnet motors for automotive applications: On one hand, to address the core issues of insufficient cooling system efficiency and susceptibility to excessive temperature rise in current automotive permanent magnet motors, we will further develop high-efficiency cooling systems tailored for high-power-density scenarios. By optimizing cooling structure design to enhance heat dissipation performance, we aim to resolve the constraints on operational reliability imposed by excessive motor temperature rise at the engineering application level. On the other hand, theoretical research will delve into collaborative design methodologies for cooling channel parameters and coolant flow velocity. This will establish quantitative correlation models between parameters and cooling performance, forming a theoretical framework to guide engineering practice. This approach will provide scientific and precise theoretical support for rapid design of cooling channels in automotive permanent magnet motors, advancing research outcomes from scenario-specific optimization to universal design methodologies.

References

[1] Z. G. Shao., *et al*., Development status and prospect of hydrogen energy and fuel cell, *Proc. Chin. Acad. Sci, 34* (2019), pp. 469-477

[2] X. Wang., *et al.*, A critical review on thermal management technologies for motors in electric cars, *Applied thermal engineering, 201* (2022), pp. 117758

[3] W. Zhao., *et al*., Analysis of a Novel Surface-Mounted Permanent Magnet Motor With Hybrid Magnets for Low Cost and Low Torque Pulsation. *IEEE Transactions on Magnetics, 57* (2021), 6, pp. 1-4

[4] W. Chen., *et al*., Water cooling structure design and temperature field analysis of permanent magnet synchronous motor for underwater unmanned vehicle. *Applied Thermal Engineering, 240* (2024), pp. 122243

[5] F. Mahmouditabar., *et al*., Design and Analysis of Interior Permanent Magnet Motor for Electric Vehicle Application Considering Irreversible Demagnetization. *IEEE Transactions on Industry Applications, 58* (2022), pp. 284-293

[6] Y. H. Lee., *et al*., A Novel Variable Flux Spoke Permanent Magnet Motor With Swiveling Magnetization for Electric Vehicles. *IEEE Access, 10* (2022), pp. 62194-62209

[7] B. Liu., *et al*., Cooling Design and Temperature Field Analysis of Radial-axial Magnetic Bearings. *Proceedings of the CSEE, 44* (2024),pp. 4945-4955

[8] M. Gulec., *et al*., Magneto-Thermal Analysis of an Axial-Flux Permanent-Magnet-Assisted Eddy-Current Brake at High-Temperature Working Conditions. I*EEE Transactions on Industrial Electronics, 68* (2021), 6, pp. 5112-5121

[9] G. Yang., *et al*., Numerical Simulation on the Flow and Temperature Field in the High-Power Motor. *IEEE Access,* 11 (2023), pp. 82830-82837

[10] Y. Xu., *et al*., Study of Thermal Field Analysis Methods of Oil-Filled Motors. *IEEE Transactions on Applied Superconductivity,* 34 (2024), 8, pp. 1-5

[11] Y. Guo., *et al*.,. A real-time temperature rise prediction method for PM motor varying working conditions based on the reduced thermal model. *Case Studies in Thermal Engineering,* (47) 2023, pp. 103098

[12] H. Zhou., et al., Rapid Prediction of Magnetic and Temperature Field Based on Hybrid Subdomain Method and Finite-Difference Method for the Interior Permanent Magnet Synchronous Motor. IEEE Transactions on Transportation Electrification, 10 (2024), 3, pp. 6634-6651

[13] S. Li., *et al*., General Analytical Model for Electromagnetic-Thermal Bi- Directional Coupling of IPM Motors in Electric Vehicles Considering Different Rotor Structures. *IEEE Transactions on Vehicular Technology,* 73 (2024), 11, pp. 16470-16480

[14] L. K. Wang., *et al*., Study on Fluid Solid Coupling Heat Transfer of Compressor Water Cooled Permanent Magnet Synchronous Motor Rotor in Rotating State. *Proceedings of the CSEE, 41* (2021), pp. 7830-7841

[15] W. Tong., *et al*., Loss and Thermal Analysis for High-Speed Amorphous Metal PMSMs Using 3-D Electromagnetic-thermal Bi-Directional Coupling. *IEEE Transactions on Energy Conversion, 36* (2021), 4, pp. 2839-2849

[16] Q. Gao., *et al*., Loss Calculation, Analysis, and Separation Method of 550 000 r/min Ultrahigh-Speed Permanent Magnet Motor. *IEEE Transactions on Industrial Electronics, 70* (2023), 4, pp. 3471-3481

[17] W. Li., *et al*., Thermal Analysis of the Solid Rotor Permanent Magnet Synchronous Motors With Air-Cooled Hybrid Ventilation Systems. *IEEE Transactions on Industrial Electronics*, *69* (2022), 2, pp. 1146-1156

[18] R. Xu., *et al*., Heat Transfer Performance Improvement of Permanent Magnet Synchronous Linear Motor Based on Embedded Staggered Double Channel Water-Cooling Structure. *IEEE Transactions on Transportation Electrification*, *10* (2024), 4, pp. 10158-10168

[19] A. Acquaviva., *et al*., Design and Verification of In-Slot Oil-Cooled Tooth Coil Winding PM Machine for Traction Application, *IEEE Transactions on Industrial Electronics, 68* (2021), 5, pp. 3719-3727

[20] P. Liang., *et al*., Water Jacket and Slot Optimization of a Water-Cooling Permanent Magnet Synchronous In-Wheel Motor. *IEEE Transactions on Industry Applications, 57* (2021), 3, pp. 2431-2439

[21] Q. Chen., *et al*., Analysis of Temperature Field and Water Cooling of Outer Rotor In-Wheel Motor for Electric Vehicle. I*EEE Access*, *7* (2019), pp. 140142-140151

[22] K. Zhang., *et al*., Design and Experimental Study of Water Cooling System for External Rotor Permanent Magnet Synchronous Motor. *IEEE Access*, *12* (2024), pp. 88034-88047

[23] X. Fan., *et al*., Water cold plates for efficient cooling: Verified on a permanent-magnet machine with concentrated winding. *IEEE Transactions on Industrial Electronics*, *67* (2019), 7, pp. 5325-5336

[24] C. Chu., *et al*., Application and Verification of Spiral Water Cooling for Rotor in High-Power Density Motors. *IEEE Transactions on Transportation Electrification, 11* (2025), 1, pp. 1245-1256

[25] GK. Pandey., *et al*., Thermal mapping and heat transfer analysis of an induction motor of an electric vehicle using nanofluids as a cooling medium. *Sustainability*, *15* (2023), 10, pp. 8124.

[26] S. Madhavan., *et al*., Thermal management analyses of induction motor through the combination of air-cooling and an integrated water-cooling system. *Scientific Reports*, *13* (2023), 1, PP. 10125.

Received: 23.5.2025.

Revised: 11.9.2025.

Accepted: 15.9.2025.